Simulating multimodal floc size distributions of suspended cohesive sediments with lognormal subordinates: Comparison with mixing jar and settling column experiments

Xiaoteng Shen [a, b, *], Erik A. Toorman [a], Michael Fettweis [c],

Byung Joon Lee [d], Qing He [b]

[a] *Hydraulics Laboratory, Department of Civil Engineering, KU Leuven, Kasteelpark Arenberg 40, B-3001 Leuven, Belgium*

[b] *State Key Laboratory of Estuarine and Coastal Research, East China Normal University, Shanghai 200062,China*

[c] *Operational Directorate Natural Environment, Royal Belgian Institute of Natural Sciences, Rue Vautier 29, 1000 Brussels, Belgium*

[d] *School of Construction and Environmental Engineering, Kyungpook National University, 2559 Gyeongsang-daero, Sangju, Gyeongbuk 742-711, Korea*

[*] Corresponding author. Hydraulics Laboratory, Department of Civil Engineering, KU Leuven, Kasteelpark Arenberg 40, B-3001 Leuven, Belgium.
E-mail addresses: xiaoteng.shen@kuleuven.be (X. Shen).

Abstract

The Floc Size Distributions (FSDs) of suspended fine-grained sediment flocs play a prime role to estimate their own fate and the transport of contaminates attached to the flocs. However, developing an efficient flocculation model that is capable of simulating continuous and multimodal FSDs is still a challenge. Recently, the population balance equation solved by the Quadrature-Based Method of Moments (QBMM) with lognormal kernel density functions has been developed to investigate the aggregation and breakage processes. It coincides with some recent observations which describe a measured FSD in coastal waters with a set of constituted lognormal distributions. The newly developed lognormal QBMM was tested with several ideal flocculation kinetic kernels, none of which, however, was used for interpreting cohesive sediment dynamics. Therefore, it raised our interest to evaluate the model performance for fine-grained sediments in shear turbulence dominated environments. In this study, additional validations against two kaolinite laboratory experiments were tested in the framework of the extended QBMM. It is hypothesized that these subordinate lognormal distributions share the same value of standard deviation. Different from the previous methods, the common standard deviation is determined empirically to reduce the number of tracers and better represent the FSDs. With sediment flocculation kinetics, the predicted FSDs reasonably reproduce the FSDs observed in both the mixing chamber and the settling column experiments. Despite the lacking of explicit descriptions of microbial effects at the current stage, this model has the potential to be implemented into large-scale particle transport models and deserves a more in-depth study in the future.

Keywords: population balance equation; cohesive sediments; floc size distribution; subordinate lognormal distributions; mixing jar; settling column

1. Introduction

Large amounts of suspended particles, such as minerals from physico-chemical and biogenic origin (e.g., clays, quartz and carbonates), living and non-living organic matters (e.g., plankton and detritus) and anthropogenic cohesive particles (e.g., microplastics), are trapped on mudflats, in navigational channels and on continental shelves each year. For example, about 480 million ton suspended sediments are annually loaded from the Yangtze (Changjiang) River in China (Song et al., 2013) of which 40% may be deposited in the estuary (Milliman et al., 1985). The reason why such small particles can deposit in these high-energy turbulent environments is obviously flocculation. That is, the component microparticles, often covered by biofilm, collide and combine with each other, and as a consequence are aggregated into clusters having larger size, decreased density and higher settling velocities than their individual constituents. The flocculation kinetics can also modulate sediment bed exchanges and determine concentration dynamics (Letter and Mehta, 2011). Thus, it is critical to understand how these processes respond to various environmental factors in natural (both freshwater and saltwater) systems, since it controls the fate of the particles themselves, and further to the toxic substances attached to the flocs. Freshwater flocs in the river are not necessarily smaller than flocs in saline water environments, since stronger shear stresses in the estuary may be the dominant effect to control the floc size (e.g., along the Yangtze River, see Guo and He, 2011; He et al., 2015). Pronounced differences of floc sizes within a tidal cycle, between spring-neap cycles, or under stormy and calm weather conditions, also highlight the role of turbulent shear in the flocculation process (Guo et al., 2017, 2018). On the other hand, Cartwright et al. (2009) point out that in the York River estuary the flocs in the biologically-dominated mud site (where bioturbation is more prevalent, see Schaffner et al., 2001) have higher settling velocities than that in the physically-dominated site (where physically-induced layering is more commonly observed within the bed), which emphasizes the effects of bioactivities on flocculation.

Flocs may range from microscopic (micron) size up to visible particles in units of millimeters, with a total size range of four orders of magnitude. Thanks to recently developed non-intrusive instruments such as the LISST (Laser In Situ Scattering and Transmissometry, see Agrawal and Pottsmith, 2000) and various digital camera systems (Benson and French, 2007; Cartwright et al., 2013; Eisma et al., 1990; Graham and Nimmo Smith, 2010; Keyvani and Strom, 2014; Manning, 2004; Shen and Maa, 2016a; Tang and Maggi, 2015), the Floc Size Distributions (FSDs) by particle volume or number can be better observed. Nevertheless, although large-scale field observations are the preferred way to study the sediment transport for engineering and environmental issues, they are hampered by high cost and geographical spreading. A coupled hydrodynamic and sediment transport model can complement measurements to cover the entire study domain. However, currently available three-dimensional (3-D) models are still not able to make satisfying quantitative predictions of sediment properties. This raises the following question: Can we do any better for the large-scale modeling of fine-grained sediment transport (Toorman, 2012)? Actually, implementing a flocculation model (with the ability to predict the temporal and spatial varying FSDs) in sediment transport models, despite the challenge, could be a solution. One difficulty is that the typical issues we focus on have cell sizes in the order of 0.1 – 10 m in the vertical and 10 – 1000 m in the horizontal, and have time steps in the order of 0.1 – 10 minutes, whereas the particle micro-behaviors such as aggregation and breakage occur at smaller scales which are resolved at a sub-grid scale with a refined spatial resolution and a reduced time step. This limits the performance of some mesoscale simulations (e.g., Lattice Boltzmann model, see Zhang et al., 2016, 2017) applicable in large study domains. In reality, it requires that the flocculation model is at reasonable cost, and that it has the potential to be extended to include other floc parameters besides the floc size, such as floc density (or fractal dimension), floc shape and floc composition that also influence the settling velocities of in-situ biomineral aggregates (Fettweis and Lee, 2017).

One candidate of such flocculation model is the Population Balance Equation (PBE) that is capable of tracking the number density n (L, $\boldsymbol{x}$, t) for particles with size L at location $\boldsymbol{x} = \boldsymbol{x}$ (x, y, z) and time t. Floc-growth based single-group PBEs (Winterwerp, 1998, 2002), class-based two- or three-group PBEs (Lee et al., 2011, 2014; Shen et al., 2018a, 2018b) and quadrature-based multi-group PBEs (Prat and Ducoste, 2006; Shen and Maa, 2015, 2016b, 2017) are among a few applications that are successfully coupled with hydrodynamics at least in one-dimensional (1-D) applications. The floc-growth based PBEs only track the representative size of all the particles, and thus is unable to address multimodal FSDs which nevertheless are commonly observed in estuaries and coastal waters (e.g., Manning and Dyer, 2002; Benson and French, 2007; Verney et al., 2011). By comparisons with several analytical cases, Marchisio et al. (2002) indicates that quadrature-based PBEs are more desirable than class-based multi-class PBEs after investigating both the computational time and the accuracy of the representative sizes. Quadrature-based PBEs also have the advantages of including any measured initial FSD (e.g., Shen and Maa, 2016b) or including more particle properties (e.g., Vale and McKenna, 2005). Nevertheless, standard quadrature-based PBEs still lack thorough comparison with field data, especially for multimodal FSDs.

Lee et al. (2012) analyzed a large number of in-situ FSDs by floc volumes collected from the Belgian coastal zone and concluded that the observed FSDs can be approximated best by four lognormal distributions for primary particles (0.1 - 4 μm), microflocs (4 - 20 μm), macroflocs (50

- 200 μm) and megaflocs (> 200 μm). The two-class PBE can efficiently and reasonably simulate the representative sizes of microflocs (with primary particles merged) and macroflocs (with megaflocs merged) (Lee et al., 2011, 2014). Later, Shen et al. (2018a, 2018b) extended the two-class model into three-class by adding an additional group to better address the appearance of megaflocs especially during algae bloom period. The simplified two-class or three-class models have also been successfully coupled with the open TELEMAC modeling system. In their model, however, only the representative sizes of the component lognormal FSDs are involved. That is, the simulated FSDs are not continuous, since they do not contain the prediction of the standard deviation of each lognormal FSD. This leads to the missing of a direct representation of the entire FSD shape.

This weakness is a challenge to be dealt with until Nguyen et al. (2016) solved the FSDs using the Extended Quadrature-Based Method of Moments (Extended QBMM or E-QBMM) (Yuan et al., 2012) with lognormal kernel density functions (Madadi-Kandjani and Passalacqua, 2015). However, only simple conceptual aggregation and/or breakage kernels within zero-dimensional (0-D) frameworks are tested and compared with the reference work by Vanni (2000). The tested kernels are not realistic for describing collision and breakage processes of cohesive aggregates in natural aquatic environments. It is not clear whether the prediction of FSDs of estuarine mud will benefit from their contributions. Therefore, the objective of this study is to conduct additional validations for the flocculation processes of cohesive sediments. The common standard deviation of the constituted FSDs is determined empirically. Two experiments are employed to evaluate the model performance: (1) a kaolinite mixing jar test by Shen and Maa (2016a) as a 0-D validation case, and (2) a kaolinite settling column experiment by Maggi et al. (2007) as a vertical 1-D validation case. The remainder of the paper is structured as follows:

Section 2 briefly introduces the PBE, the E-QBMM and the solution methods. Section 3 mainly describes two experiments for model validations. The results and discussion on model predictions are carried out in Section 4, with some thoughts on the development of a coupled hydrodynamic, turbulence and flocculation model. The conclusions are presented in Section 5.

2. Model description and solution methods

2.1 Moment transport equations

Consider the following PBE in a vertical 1-D format for describing the evolution of number density of suspended particles in a carrier fluid (Shen and Maa, 2015, 2016b, 2017):

$$\frac{\partial n(L,z,t)}{\partial t}-\frac{\partial\left[n(L,z,t)\cdot w_s(z,t)\right]}{\partial z}-\frac{\partial}{\partial z}\left(D(z)\cdot\frac{\partial n(L,z,t)}{\partial z}\right)$$

$$=\frac{L^2}{2}\int_0^L\left[\frac{\alpha\cdot\beta\left((L^3-\lambda^3)^{1/3},\lambda\right)}{\left(L^3-\lambda^3\right)^{2/3}}\cdot n\left((L^3-\lambda^3)^{1/3},z,t\right)\cdot n(\lambda,z,t)\right]d\lambda$$

$$-n(L,z,t)\int_0^\infty\alpha\cdot\beta(L,\lambda)\cdot n(\lambda,z,t)d\lambda+\int_L^\infty a(\lambda)\cdot b(L\,|\,\lambda)\cdot n(\lambda,z,t)d\lambda-a(L)\cdot n(L,z,t) \tag{1}$$

where n (L, z, t) is the number density of the particles with size L at vertical coordinate z and time t, w_s is the mass-weighted settling velocity, D is the eddy diffusivity, λ is the variable of integration with dimension of size, α is the collision efficiency, β (L, λ) is the collision frequency between particles with size L and λ, a (L) is the breakage frequency of particles with size L, and b $(L \mid \lambda)$ is the fragmentation distribution function describing the created number of particles with size L after the breakage of a parent particle with size λ. The left hand side of Eq. 1 comprise the unsteady term, the settling term and the diffusion term, respectively. The right hand side consists of the flocculation sources and sinks (Shen and Maa, 2015). The advection term may be added in Eq. 1 for strong bulk transport of sediments.

To avoid tracking a large number of size classes, the FSDs can instead be stored in their moments by the moment transformation:

$$m_k(t) = \int_0^\infty L^k n(L,t)dL \qquad (k = 0, 1, \ldots) \qquad (2)$$

in which m_k is the kth order moment of the FSD. Note that m_0, m_2 and m_3 are proportional to the total number, total surface area and total volume of the solid particles.

Substituting Eq. 2 into Eq. 1, the governing equation can be rewritten as a set of moment transport equations (Marchisio et al., 2003a):

$$\frac{\partial m_k(L,z,t)}{\partial t} - \frac{\partial\left[m_k(L,z,t)\cdot w_s(z,t)\right]}{\partial z} - \frac{\partial}{\partial z}\left(D(z)\cdot\frac{\partial m_k(L,z,t)}{\partial z}\right)$$

$$= \frac{1}{2}\int_0^\infty n(\lambda,z,t)\int_0^\infty \alpha\cdot\beta(L,\lambda)\cdot\left(L^3+\lambda^3\right)^{k/3}\cdot n(L,z,t)dLd\lambda$$

$$-\int_0^\infty L^k n(L,z,t)\int_0^\infty \alpha\cdot\beta(L,\lambda)\cdot n(\lambda,z,t)d\lambda dL$$

$$+\int_0^\infty L^k\int_0^\infty a(\lambda)\cdot b(L\,|\,\lambda)\cdot n(\lambda,z,t)d\lambda dL - \int_0^\infty L^k a(L)\cdot n(L,z,t)dL$$

$$(k = 0, 1, \ldots) \qquad (3)$$

This equation is unclosed since the FSD should be resolved from its moments to make sure that the source and sink terms are physical. The moments have to stay in the moment space, which is the reliability condition of these quadrature-based methods (Wright, 2007; Nguyen et al., 2016; Laurent and Nguyen, 2017). In fact, even a suitable closure does not necessarily guarantee a realizable FSD, especially at the boundary. Nevertheless, this issue is not always considered, since approaches that determine if a vector belongs to the moment space (characterized by the Hankel determinants) are generally unsatisfactory and computationally heavy.

2.2 Solution method and sediment flocculation kinetics

In order to close the moment transport equation (Eq. 3), Yuan et al. (2012) proposed that the number density function can be reconstructed by a weighted superposition of non-negative functions:

$$n(L) = \sum_{i=1}^{N} w_i \cdot \delta_\sigma(L, L_i) \tag{4}$$

where δ_σ (L, L_i) is the kernel density function (i.e., the subordinate FSDs), w_i and L_i are the non-negative weights and corresponding representative sizes (also referred to as "abscissas", "nodes" and "pivots") of the constituted FSDs, N is the number of component FSDs, and σ is a unique nonnegative parameter shared by all subordinate FSDs. Hereafter we drop symbol z and t in the number density function n (L) to focus on the FSD at a specific time and location.

Lee et al. (2012) concluded that an observed FSD of estuarine mud can be decomposed into two to four lognormal distributions to estimate the settling flux with 3% - 10% errors. Thus, it is straightforward to select the kernel density function δ_σ (L, L_i) as a lognormal distribution at first stage in our applications. In this sense, the parameter σ in Eq. 4 becomes the standard deviation σ of the lognormal distributions (Madadi-Kandjani and Passalacqua, 2015):

$$\delta_\sigma(L, L_i) = \frac{1}{L\sigma\sqrt{2\pi}} \exp\left[-\frac{\left(\ln(L / L_i)\right)^2}{2\sigma^2}\right] \tag{5}$$

If $\sigma \to 0$, $\lim_{\sigma \to 0} \delta_\sigma(L, L_i) = \delta(L - L_i)$, and thus Eq. 4 is reduced to:

$$n(L) = \sum_{i=1}^{N} w_i \cdot \delta(L - L_i) \tag{6}$$

which can be solved by the standard QBMM (McGraw, 1997; Shen and Maa, 2015). Note that although a continuous FSD can be approximated by a large number of delta functions in QBMM (Eq. 6), it is numerically difficult to track the FSD with high order moments. That is, strictly speaking, the FSDs predicted by the QBMM are usually limited by size classes less than eight. Selecting lognormal distributions as the kernel density functions, nevertheless, will make the entire FSD predictions truly continuous.

For an arbitrary function $g(L)$, the integral with the number density function $n(L)$ as the weight function can be expressed as (Madadi-Kandjani and Passalacqua, 2015):

$$\int_0^\infty g(L) \cdot n(L) \cdot dL = \int_0^\infty g(L) \cdot \sum_{i=1}^{N} w_i \cdot \delta_\sigma(L, L_i) dL = \sum_{i=1}^{N} \sum_{j=1}^{N_i} w_i w_{ij} g(L_{ij}) \tag{7}$$

where L_i and w_i are the primary abscissas and weights (i = 1, 2, …, N), and N is the number of subordinate lognormal functions. For each lognormal function $\delta_\sigma(L, L_i)$ (Eq. 5), L_{ij} and w_{ij} (j = 1, 2, …, N_i) are the secondary abscissas and weights. In general, $N_i \geq N$ is required in order not to lose the accuracy of introducing the second abscissas and weights.

Selecting $g(L) = L^k$, and substituting Eq. 7 into Eq. 3, the governing equation can be expressed as:

$$\frac{\partial m_k}{\partial t} - \frac{\partial (m_k \cdot w_s)}{\partial z} - \frac{\partial}{\partial z}\left(D \cdot \frac{\partial m_k}{\partial z}\right)$$

$$= \frac{1}{2} \sum_{i_1=1}^{N} \sum_{j_1=1}^{N_i} w_{i_1} w_{i_1 j_1} \sum_{i_2=1}^{N} \sum_{j_2=1}^{N_i} w_{i_2} w_{i_2 j_2} \alpha \cdot \beta(L_{i_1 j_1}, L_{i_2 j_2}) \cdot ({L_{i_1 j_1}}^3 + {L_{i_2 j_2}}^3)^{\frac{k}{3}}$$

$$-\sum_{i_1=1}^{N}\sum_{j_1=1}^{N_i} L_{i_1j_1}{}^{k} w_{i_1} w_{i_1j_1} \sum_{i_2=1}^{N}\sum_{j_2=1}^{N_i} w_{i_2} w_{i_2j_2} \alpha\cdot\beta(L_{i_1j_1}, L_{i_2j_2})$$

$$+\sum_{i=1}^{N}\sum_{j=1}^{N_i} w_i\cdot a_{ij}(L_{ij})\cdot\overline{b_{ij}}^{(k)}\cdot w_{ij} - \sum_{i=1}^{N}\sum_{j=1}^{N_i} w_i\cdot L_{ij}{}^{k}\cdot a_{ij}(L_{ij})\cdot w_{ij} \qquad (k=0,1,\ldots) \tag{8}$$

with $$\overline{b_{ij}}^{(k)} = \int_0^\infty L_{ij}{}^{k} b(L\mid\lambda)dL \tag{9}$$

At each location and time step, the FSD, i.e., the L_i (i = 1, …, N) and w_i (i = 1, …, N) are reconstructed from the moments m_k, which is referred to as "moment inversion" (e.g., Passalacqua et al., 2018). It is important to note that in Lee et al. (2012)'s study, the parameter σ varies for each constituted distribution for a better match of the fitted and measured FSDs; in this study, however, σ is shared for all subordinate lognormal distributions. With the parameter σ properly selected, the predictions of the entire FSDs are not significantly deviated (Fig. 1). A common σ can also reduce the number of tracers. For example, as shown in Fig. 1, if using number of N lognormal FSDs to approximate the measurement, an unshared σ requires $3N$ variables while a common σ requires only $2N$+1. If the common σ is further determined empirically (Eq. 10) rather than treated as an independent tracer, the number of tracers is reduced to $2N$. It is hypothesized that the standard deviation (σ) of the subordinate distribution is enlarged with the increment of the characteristic mean size d_{32} until an equilibrium or quasi-equilibrium state. At t = 0, all particles are assumed concentrated on single size primary particles with σ = 0. Thus, the common σ is given by:

$$\sigma = \alpha_0\cdot\ln\left(\frac{d_{32}}{l_p}\right) \tag{10}$$

where d_{32} ($d_{32} = m_3/m_2$) is the Sauter mean size (Mugele and Evans, 1951; Sowa, 1992), l_p is the size of primary particles and α_0 is a fitting constant.

The kth order moments of the lognormal distribution δ_σ (L, L_i) are (Magnus et al., 1996):

$$m_k(L_i,\sigma)=\exp\left(k\cdot\ln L_i+k^2\cdot\sigma^2/2\right) \tag{11}$$

Let $Z=\exp\left(\sigma^2/2\right)$, Eq. 2 becomes:

$$\begin{cases} m_0=w_1+w_2+...+w_N=m_0^{\ *} \\ m_1=Z(w_1L_1+w_2L_2+...+w_NL_N)=Z\cdot m_1^{\ *} \\ m_2=Z^4(w_1L_1^{\ 2}+w_2L_2^{\ 2}+...+w_NL_N^{\ 2})=Z^4\cdot m_2^{\ *} \\ \cdots \\ m_k=Z^{k^2}(w_1L_1^{\ k}+w_2L_2^{\ k}+...+w_NL_N^{\ k})=Z^{k^2}\cdot m_k^{\ *} \end{cases} \tag{12}$$

(k = 0, 1, …)

After the common standard deviation σ being found in Eq. 10, the first 2N terms in Eq. 12 can be employed to solve L_i and w_i (i = 1, …, N):

$$\sum_{i=1}^{N} w_i L_i^{\ k}=m_k^{\ *} \qquad \left(k=0,1,...,2N-1\right) \tag{13}$$

Eq. 13 can be solved by the Chebyshev algorithm given by Wheeler (Wheeler, 1974; Su et al., 2007; Yuan and Fox, 2011; Shen and Maa, 2015). The main point of Eq. 13 is to find the eigenvalues and eigenvectors of a real, symmetric, tri-diagonal Jacobi matrix, with the elements of the matrix computed by the moments from a three term recurrence relation, which is based on the theory of orthogonal polynomials. Although Eq. 13 is numerically ill-posed, it is practical to apply standard QBMM to solve it for low order moments ($N\leq 4$). An adjustable factor may be included only when more subordinate lognormal distributions are required.

Therefore, the solution of governing equation (Eq. 8) can be summarized in the following:

(a) At t = 0, compute the initial 2N moments m_0, m_1, …, m_{2N-1} for a given initial particle size distribution (Eq. 2), assuming using number of N subordinate lognormal distributions to approximate the entire FSD.

(b) Update the moments, by solving the advection (if necessary), diffusion and settling terms in Eq. 8.

(c) Estimate the common standard deviation σ (Eq. 10), and extract the primary abscissas L_i and weights w_i (i = 1, …, N) from the first 2N moments m_k (k = 0,1,…,2N−1) (Eq. 13), using Wheeler's algorithm (for unknown kernel density functions).

(d) Find the secondary abscissas L_{ij} and w_{ij} (j =1, 2, …, N_i) for each constituted lognormal FSD δ_σ (L, L_i), using Gauss-Stieltjes-Wigert quadrature (equivalent to use Wheeler's algorithm for lognormal kernel density functions).

(e) Calculates the source and sink terms in Eq. 8, updates the moments, and go to (b) to solve the transport equation for the next time step.

In order to address the cohesive sediment properties by solving Eq. 8, the flocculation kinetics are selected based on previous studies (e.g., Smoluchowski, 1917; Winterwerp, 1998; Marchisio et al., 2003b; Maggi et al., 2007; Shen and Maa, 2015, 2016b):

Collision frequency: $$\beta(L_{i_1 j_1}, L_{i_2 j_2}) = \frac{G}{6}(L_{i_1 j_1} + L_{i_2 j_2})^3 \quad (14)$$

Breakage frequency: $$a(L_{ij}) = E_b \cdot \left(\frac{\mu}{F_y}\right)^{1/2} \cdot G^{3/2} \cdot L_{ij} \cdot \left(\frac{L_{ij}}{l_p} - 1\right)^{3-nf} \quad (15)$$

Fragmentation distribution function:

$$\overline{b_{ij}}^{(k)} = L_i^{\,k} \cdot K^{(3-k)/3} \quad (16)$$

where G is the shear rate, E_b is the breakage fitting parameter, F_y is the floc strength, and K describes the number of daughter flocs created after a parent floc breaks up.

The settling velocity for each size group is represented as (Winterwerp, 1998):

$$w_{s,i} = \Phi_{HS} \frac{1}{18} \frac{(\rho_s - \rho_w)g}{\mu} l_p^{3-n_f} \frac{L_i^{n_f - 1}}{1 + 0.15 \cdot Re_f^{0.687}} \quad (17)$$

where ρ_s and ρ_w are the densities of sediment and water, n_f is the fractal dimension of flocs, μ is the fluid dynamic viscosity, g is the gravitational acceleration, and $Re_f = w_{s,i} \cdot L_i \cdot \rho_w / \mu$ is the floc particle Reynolds number. The parameter $\Phi_{HS} = \left(1 - \frac{c}{c_{gel}}\right)^A$ is the correction factor accounting for hindered settling (Cuthbertson et al., 2008), where $c \propto L^3$ is the Suspended Sediment Concentration (SSC), c_{gel} is the gelling concentration, and A is a constant between 2.5 − 5.5 and set as 4.7 (Richardson and Zaki, 1954).

3. Case studies

3.1 Case 1: Mixing jar experiments

Recently a laboratory experiment was carried out by Shen and Maa (2016a) to investigate the equilibrium FSDs of suspended kaolinite in a five liter cubic mixing chamber for different sediment concentrations, shear rates, salinities and guar gum dosages. The LIGHTNIN A310 propeller was used to generate the turbulence. The tank averaged shear rate G was controlled by the rotational speed of the propeller (N_r) which was driven by a DC gear motor, and G was also influenced by the properties of the propeller as well as the volume of the chamber V_c (Ducoste and Clark, 1998):

$$G = \sqrt{\frac{\rho_w N_r D_r N_{rp}}{\mu V_c}} \quad (18)$$

in which D_r is the diameter of the propeller and N_{rp} is a propeller specific constant. Sediment samples were extracted by syringe and weighted after oven-dried overnight to determine the sediment concentration (c). The FSDs were observed by a camera and image processing system, with a resolution of 2×2 pixels to identity a floc with minimum size of 5 μm. The camera continuously took pictures every 2 s, with the camera and light source trigger controlled by a programmed microcontroller Teensy 2.0. The FSDs at steady state are reported by an average of a continuous one hundred images. The image processing procedure was supported by comparison with commercially available particles (Shen and Maa, 2016a), and later was also reported as "well correlated" with other image capturing systems (Ramalingam and Chandra, 2017). Such a mixing chamber and image processing system was placed at Virginia Institute of Marine Science (USA) from 2013 to 2015.

Shen and Maa (2016a) have successfully modeled the FSDs in most cases using the standard QBMM. However, for cases of sediments with guar gums, a strong bimodal FSD were observed. Their method cannot address the second peak of FSD with a maximum of eight nodes. In this study, the FSDs were instead estimated by two subordinate lognormal distributions ($N = 2$). For each subordinate distributions, a three-node quadrature was used to estimate its moments ($N_i = 3$). The settling and diffusion terms in Eq. 8 are neglected to address the average property in the mixing chamber. The initial kaolinite concentration (c) was 0.52 g/L, the tank-averaged shear rate (G, calculated by Eq. 18) was 55 s^{-1}, and the guar gum concentrations $c_{guar} = \{0, 5, 10, 15, 20, 30\}$ mg/L. For each case, the jar test was carried out independently, and the solution was discarded before the next test. The propeller rotated at its maximum speed for half an hour to destroy the flocs, and then was set to the proposed rotational speed to promote flocculation. Thus, all the particles are assumed in the form of primary particles at $t = 0$ with $l_p = 6$ μm. The steady state FSDs were used to calibrate this model.

3.2 Case 2: Settling column experiments

The second validation is to compare the model results with FSD measurements in a settling column experiment by Maggi et al. (2007). The settling column was designed and manufactured at Delft University of Technology (Netherlands), with height 5 m (totally 4 m, from surface to 1 m above bottom) and diameter 30 cm. A homogeneous and isotropic turbulent field was generated by an oscillating grid over the settling section of the column height (e.g., Cuthbertson et al., 2010, 2018; Tang and Maggi, 2015). By comparison with several grid configurations, Maggi (2005) proposed that the rectangular grid was the optimal selection to compromise both the flow hydrodynamic behavior and the manufacturing costs. Driving systems controlled the movement of the grid with a maximum stroke (A_0) of 8.4 cm. The shear rate G was linearly correlated and controlled by the grid frequency, with shear rate G = {5, 10, 20, 40} s^{-1} corresponding to grid frequency f_g = {0.05, 0.1, 0.25, 0.5} Hz, respectively. The aggregates passed through the settling section and reach the measuring section which was located at 0.5−1 m above bottom. A small fraction of the flocs were transferred to a collector, with the FSDs measured by a digital camera without being affected by large-scale water circulation in the settling column. The aggregates are illuminated by a laser source and captured in the images with a resolution of 6 μm per pixel. The bottom 0.5 m was the bed section, with particles passing through the settling and measuring sections deposited on the bottom. In the experiment, kaolinite suspensions with concentrations c ± 0.015 g/L were maintained by a buffer tank on the top of the settling column. By assuming the downward flux above and below the measuring section are close, this flocculation process of suspended kaolinite can be simulated using a 0-D model (Maggi et al., 2007; Mietta et al., 2008; Shen and Maa, 2015). However, this assumption cannot be verified or argued without additional measurements. In this section, a vertical 1-D model (Eq. 8) was employed to reproduce the experiment, with sediment mass concentration 0.5 g/L at the top boundary and shear rates 5, 10, 20 and 40 s^{-1} respectively. Although the vertical eddy diffusivity D was not reported in their experiment, van Leussen (1994) pointed out that its value in such experiment can be determined by the following relationship:

$$D = \alpha_g \cdot f_g \cdot A_0^2 \tag{19}$$

in which α_g is a constant that should be determined from the experiment. Here, it hypothesized that the energy from the grid bars is dissipated by the fluid of the whole cross section. Therefore, α_g can be estimated by the ratio of grid bar areas to the cross section of the settling column. It results in $\alpha_g = 0.19$. This value is similar to van Leussen's experiment with the settling column having similar column diameter and grid configuration. It is understandable that the energy will be dissipated rapidly when flocs settled out of the turbulent section, and thus it also assumes that the eddy diffusivity and the energy dissipation rate rapidly decreases to their minimum value from the settling-measuring section interface (i.e., 1 m above the bottom) to the bed. The initial and boundary conditions are in accordance with the following assumptions: (1) at $t = 0$, all particles are primary particles with size of 8 μm; (2) at the upper boundary, the sediments released from the buffer tank are all primary particles with a fixed concentration of 0.5 g/L; (3) at the lower boundary, sediments are freely deposited without erosion and resuspension; (4) the standard deviation σ in the bottom cell is set to 0 to avoid numerical instabilities. Finally, the observed FSDs at the measuring section are used to calibrate and validate the model.

4. Results and discussion

4.1 Comparison with mixing jar experiments: 0-D test

The parameters for different guar gum concentrations c_{guar} = {0, 5, 10, 15, 20, 30} mg/L are summarized in Table 1. A value of K = 5 is selected in the fragmentation distribution function (Eq. 16) for all cases. The errors (E) of predicted and observed FSDs are evaluated using the following equation (Maggi et al., 2007; Shen and Maa, 2017):

$$E = \frac{1}{2}\left(\sum_i \left|w_{M,i} - w_{E,i}\right|\right) \tag{20}$$

In this experiment, the measured number frequencies are given at L_E = {5.27, 7.33, 10.2, 14.2, 19.8, 27.6, 38.4, 53.5, 74.5, 104, 144, 201, 280, 390, 543, 756, 1052} μm. Thus, the differences of modeled w_M and experimental w_E at diameter L_E are evaluated using Eq. 20, with $\sum_i w_{M,i} = 1$ and $\sum_i w_{E,i} = 1$.

The simulated FSDs agree well with the measurements for all guar gum dosages (Fig. 2), with a maximum error of 0.07 (Table 1). Enhanced model predictions are achieved in this study, compared with the previous study by Shen and Maa (2016a) that failed to mimic the bimodal FSDs using an eight-node QBMM. Two subordinate lognormal distributions (N = 2) of microflocs and macroflocs are employed to represent the entire FSD. This selection is not only for reducing the number of tracers. Notice that a better prediction is not always guaranteed by increasing the number of subordinate FSDs. It is influenced by the properties of the flocculation kinetics. Not all the target FSDs are decomposable into lognormal distributions. Also, it is not suitable to use a large number of component FSDs to approximate a simple distribution. For example, when no guar gum is added, it seems that the target FSD may be better predicted by one lognormal distribution instead of two (Fig. 2(a)). Based on the above concerns, N = 2 for L_1 represents microflocs and L_2 represents macroflocs are employed for all cases in this study.

The breakage coefficient E_b is in the order of 10^{-6} in this case, about one order of magnitude lower than clean sediment for a reduced breakage because of organic matter (Table 1). The ratio of α/E_b is a critical parameter to exhibit floc growth (Mietta et al., 2011; Furukawa and Watkins, 2012; Shen and Maa, 2016b). A maximum ratio of α/E_b are occurred for guar gum concentration 15 mg/L (Fig. 3(a)), with maximum size of macroflocs (L_2 = 151 μm, Fig. 3(c)) and highest weights (w_2 = 0.69, Fig. 3(d)) also at this dosage. It confirms the existence of an optimal c_{guar} dosage (Table 1) for settling flocs in natural environment or waste water treatment. The sizes of microflocs L_1 are close to each other (~ 32 μm, Fig. 3(c)), with its minimum weight (w_1) also at c_{guar} = 15 mg/L (Fig. 3(d)). The fractal dimension n_f has the smallest value also at this optimal c_{guar} dosage (Fig. 3(b)). An average fractal dimension of 2.7 (Table 1) indicates that the flocs in the mixing chamber, although with size enlarged, are still relatively compact. In our sensitivity test, a fractal dimension n_f from 2.0 to 2.7 will not significantly alter the size of the major peak; however, the common standard deviation σ is reduced as n_f deceases (Fig. 4(a)). A high n_f will decrease the breakup frequency (Eq. 15), which lead to higher mean size and larger σ. It is essential to note that a common σ derived from the (2N)th moment (Madadi-Kandjani and Passalacqua, 2015) will lead to numerical instability and physically to a narrow spread of FSD in our applications, and thus is not used. With an empirical σ (Eq. 10) related to the mean size of FSD, a better estimation of the spread of FSD are reached. Although the selected α_0 (Eq. 10) and thus σ are close in all cases (Fig. 3(b)(d)), the predicted FSDs are sensitive for the selection of α_0 (Fig. 4(b)). Increase of the value of α_0 will increase σ straightforwardly, and therefore make the spread of FSD wider and decrease the size of main peak (Fig. 4(b)).

Taking c_{guar} = 15 mg/L as an example, the steady state is achieved after 2 hrs according to the model (Fig. 5(a)). The total particle number m_0 reduced to 0.015 ‰ of initial m_0 at steady state.

The total particle volume m_3 was unchanged for volume conservation in 0-D model. The moments m_1 and m_2 decrease with time until arriving at steady state, since aggregation dominates at the beginning and breakage becomes comparable with aggregation after large floppy flocs occurring. The fourth moment m_4 is integrated from the simulated FSDs at each time step. For spherical particles, m_4 is proportional to the total surface area of particles settling per unit time (Mehta, 2013). Therefore, they are increased due to flocculation until a steady state. The time evolutions of FSDs are displayed every 15 minutes until steady state (Fig. 5(b)). It shows how a bimodal FSD generated from point distributed primary particles. Firstly, the major peak remains close while the standard deviation rapidly increases to yield a wider distribution. After that, the major peak swifts to the right side and microflocs dominated because of aggregation. Then, a second peak becomes obvious with time, indicating the occurrence of large macroflocs. The effect of breakage become important, since larger flocs with more constitute primary particles are easier to destroy. Finally, the aggregation and breakage arrive at equilibrium to form a FSD with two major peaks.

4.2 Comparison with settling column experiment: 1-D test

By trial-and-error, the coefficients $\alpha = 0.95$ and $E_b = 1.05 \times 10^{-5}$ were selected to best fit the FSDs observed at the measuring section ($Z = 0.75$ m). The parameter α_0 which controls the spread of simulated FSDs (Eq. 10) was set as 0.195. Other parameters for the best-quality simulations are summarized in Table 2. The case of shear rate $G = 10$ s^{-1} was used for calibration, while $G = \{20, 40\}$ s^{-1} were adopted for validation. It can be shown that the predicted and observed FSDs at the measuring section reasonably match for $G = \{10, 20, 40\}$ s^{-1} (Fig. 6). It shows a significant improvement in comparison with that given by Maggi et al. (2007) or Shen and Maa (2015). The fitted FSDs in Fig. 6 are based on a superposition of two lognormal constituted FSDs with different variances by the software DistFit (Chimera Technologies, USA) to better represent the observations. Notice that for $G = 5\ \mathrm{s}^{-1}$, the low oscillating frequency ($\sigma_g < 0.1$ Hz) might lead to a non-homogenous mixing (Maggi, 2005). Therefore, a reasonable agreement was only attained by recalibrating the model by a larger collision efficiency $\alpha = 1.1$ whereas a smaller variance with $\alpha_0 = 0.175$ (Fig. 6(d)). Note that by definition the α should be less than unity; however, $\alpha > 1$ is possible for flocs with low fractal dimensions (Lee et al., 2000; Shen and Maa, 2015). For all the cases, the major peaks of the FSD are properly addressed against measured value, while the secondary peaks for the macroflocs are more or less deviated from the observations. This is because of the assumption of a common standard deviation σ. The common σ should compromise a large σ of microflocs and a small σ of macroflocs in this application.

For $G = 10\ \mathrm{s}^{-1}$, the vertical profiles of SSC, weighted settling velocity w_s, total particle number m_0 and the arithmetic mean diameter $d_{1,0}$ ($d_{1,0} = m_1/m_0$) along the column are examined. The SSC in the upper column decreases as particles are aggregated and settled to the lower section (Fig. 7(a)). Although sediments at the top are operated by a buffer tank to maintain a constant SSC around 0.5 g/L, a minimum SSC occurs close to the surface ($Z = 4.5$ m) with the SSC decreasing to half of the initial value. The concentration at the measuring section does not vary significantly, while the SSC at the bed section largely increases (> 1 g/L) since the settled large flocs pass through the measuring section and are concentrated on the bottom. At the first few minutes, the settling velocities w_s at the bed section ($Z < 1$ m) are smaller than w_s at the upper section ($Z = 1 - 4.5$ m) (Fig. 7(b)). This is because the oscillating grids only lay in the settling section, and thus shear rate is largely reduced at the bed section so that it cannot promote flocculation at the beginning. With time, however, the w_s at the bottom section increases since larger flocs are settled to the bottom, which also leads to an increase of particle diameter $d_{1,0}$ at the bed section. The deviation of settling velocity at the measuring section is small, and the w_s gradually decreases until the surface where primary particles are released from the buffer tank. The relative total particle number $m_0(t)/m_0(t=0)$ decreases to 1‰ (Fig. 7(c)) in the measuring section, while the mean size $d_{1,0}$ increases to 45 μm at that location (Fig. 7(d)).

Also for $G = 10$ s^{-1}, the variation of SSC is merely 5 % at the measuring section ($Z = 0.75$ m) (Fig. 8(a)), which more or less confirms the assumption of a "constant" sediment concentration. At column heights at the settling section, however, the sediment concentrations obviously alter with time. During the simulating period, the concentration at $Z = \{1.75, 2.75, 3.75\}$ m continuously decreases. Close to the surface ($Z = 4.75$ m), the SSC decreases to 0.32 g/L during the first half an hour and becomes steady thereafter. At all column heights, the mean size $d_{1,0}$ increases at the beginning as particle growing, and then arrives at steady state after half an hour (Fig. 8(b)). The settling velocities w_s (Fig. 8(c)) and standard deviation σ follow the same trend of $d_{1,0}$ (Fig. 8(d)). In less flocculated areas ($Z = 4.75$ m) close to the surface, the $d_{1,0}$, w_s and σ reach equilibrium much faster than in well flocculated areas ($Z = 0.75$ m).

The FSDs against different SSCs are also predicted in Fig. 9. A higher SSC of 0.75 g/L may increase the mean diameter $d_{1,0}$ up to 57.0 μm, while a SSC of 0.25 g/L will lower $d_{1,0}$ down to 32.5 μm (Fig. 9). This is because the flocculation rate is proportional to the particle concentrations, with higher concentrations resulting in high possibilities of collision. For $G = 10$ s^{-1} with different concentrations $c = \{0.25, 0.5, 0.75\}$ g/L, the sizes of microflocs L_1 are close ($L_1 = 21.1 \pm 2.6$ μm). Larger standard deviations ($\sigma = \{0.42, 0.49, 0.54\}$) are expected for higher SSCs. Both the sizes and weights of macroflocs increase as c increases ($L_2 = \{53.1, 59.2, 62.7\}$ μm and $w_2 = \{0.27, 0.48, 0.7\}$). These predictions can be tested in future experiments.

4.3 Model evaluation

In this study, the applications of the E-QBMM are based on the observations that the in-situ FSD can be decomposed into a limited number of lognormal distributions. In general, four component lognormal FSDs are sufficient to represent a measured FSD (Lee et al., 2012) to identify groups of primary particles, microflocs, macroflocs and megaflocs. This means, only a maximum of eight tracers (i.e., their weights and representative sizes) with a common standard deviation are required in a large scale model. To further reduce the number of tracers for exhibiting a multimodal FSD, as low as four tracers can be employed as used in this study. Compared with previous two- or three-class PBEs, this model provides a straightforward percept of the entire continuous FSD instead of only discrete representative size groups. It avoids reformulation of the flocculation source and sink terms for different number of size groups, but adopts comparable number of tracers which will not significantly increase the computational demands. After validated by more field data, this model has the potential to simulate the spatially and temporally varied, continuous, and multimodal FSDs within the framework of large-scale simulations.

Although this method is efficient and powerful to deal with the entire FSD, it has a few weaknesses based on the assumptions that all the subordinate FSDs share the same standard deviation σ. The purpose of this selection is to reduce the number of tracer, and to make it possible to use the Wheeler's method to solve the "well-studied" low order non-linear equation system (Eq. 13). However, from Lee et al. (2012) we know that the standard deviations of the constituted FSDs sometimes are largely different. A single σ is merely chosen by matching the simulated and observed FSD, without exploring its physical meaning by investigating the change of σ with environmental parameters (such as shear rate, salinity, temperature and bioactivities). In fact, the standard deviation σ used to characterize the width of the distribution in the model (or in the in situ FSD) should also include non-spherical characters of the particles and is thus not only indicating different sizes of particles. Furthermore, a standard deviation σ does not always exist. Even treating σ as an additional tracer, none of the iteration methods (Madadi-Kandjani and Passalacqua, 2015), the Ridders' method (Press et al., 1992) or the Brent's method (Press et al., 1992) proposed by recent studies could guarantee a realistic σ. Physically it means that the code fails to find a single common σ to compromise all the component FSDs when more subordinates are included. Thus, $N = 2$ is a practical selection on the first stage. A standard deviation σ derived from the ($2N$)th order moment of the FSD (Madadi-Kandjani and Passalacqua, 2015; Nguyen et al., 2016; Passalacqua et al., 2018), if applicable, results in a narrow spread of FSD in our tests. This may be because m_{2N} highlights larger particles and underestimates the value of σ due to rounding-off errors. This part can be improved if a better method to find the optimal σ to minimize the simulated and measured FSDs is available. It is also noticeable that the subordinate lognormal FSD assumption is based on the data collected in well-mixed Belgian coastal zones (Lee et al., 2012; Fettweis and Lee, 2017; Fettweis e t al., 2016). Few measured data from other areas, especially stratified regions, are available to evaluate this decomposition. Another issue is that the current flocculation kinetic equations are decoupled with transport terms, and are always solved explicitly in each time step. That is, at time t, the tracer source and sink terms are estimated using the values at time $t-\mathrm{d}t$. Therefore, better numerical schemes should be developed to accommodate both explicit and implicit time stepping.

Moreover, although flocculation dynamics in rivers and estuaries is strongly dependent on microbial activities (Wolanski and Elliott, 2016), this model does not explicitly include these effects, because it may result in an endless chain of processes at the current stage. Actually, even the most recently published papers still mainly focus on clean sediments without biology (e.g., Cuthbertson et al., 2018; Mhashhash et al., 2018; Tran et al., 2018; Zhang et al., 2018; Zhu et al., 2018). In fact, even easier parts of ecosystems, such as organic matter, phytoplankton and biofilms, are still not fully understood and quantifiable. It is possible to include an ecohydraulics library, such as AED2 (the Aquatic EcoDynamics modeling library, http://aed.see.uwa.edu.au/research/models/AED/), which can be used by the TELEMAC system (http://www.opentelemac.org/), but the chance for gain in accuracy is only achieved by decreasing the involved processes, due to their high degree of empiricism and uncertainty on the model parameters. Indeed, the accumulation of errors due to parameter uncertainty may outweigh the hoped-for increase in accuracy by including more processes. This problem of overparameterization is well documented in other fields (Reichert et al., 1996; Schoups et al., 2008)

It is also critical to note that there are different methods to measure in situ FSDs but they may not give the same results. The size is only well defined if the particle is a sphere. However, natural particles are seldom spheres and have irregular shapes and this introduces - when measured - intrinsically a size distribution. If we measure the size of a large amount of the similar but irregular particles (e.g., ellipsoids), the result is a distribution. A model that has been calibrated for a LISST derived FSD will not be able to reproduce the same flocs measured by a digital camera (e.g., Mikkelsen et al., 2005), meaning that the outcome of even the best flocculation model is only as good as the measuring system that is used to collect the FSDs. The measuring technique has weaknesses that are reflected in the FSDs. Generally camera systems cannot resolve the fine particles smaller than 10 µm, while LISST has a limited size range for the fine and the very large particles. Out of range particles are influencing the size distribution. Nowadays, there is still no good way for correcting FSDs for these spurious data, but it should be aware that the very large (megaflocs) and the very small particles (primary particles) maybe under-represented or over-represented in the in situ LISST derived FSDs. In reality, even if the size distributions in situ and in the model are well resolved, there are still uncertainties involved in the estimation of the density and the settling velocity (the ultimate parameter for the model). For example, when using fractal theory to estimate the floc density, small changes in fractal dimension may induce large changes in the settling velocity. The calculation of the settling velocity is still subject to calibration (e.g., by using SSC values). Given the uncertainty of the measured FSDs, further studies are required to better represent particles from measuring points.

5. Conclusions

In this study, the multimodal FSDs of suspended cohesive sediments are successfully predicted by using the E-QBMM with sediment flocculation kinetics, assuming the target FSDs consisting of a set of subordinate lognormal distributions. The main conclusions are:

(1) Earlier studies usually fail to simulate the entire FSDs of the cohesive sediments in aquatic environments even with a large number of size classes. In this study, however, the FSDs are reasonably represented by the weight (wi) and the representative size (Li) of each component lognormal FSD, with a common standard deviation (σ).

(2) In our validations against two laboratory experiments, two subordinate lognormal distributions for microflocs and macroflocs are employed to reproduce the observed FSDs in the mixing chamber and the settling column. This selection only introduces four tracers (i.e., L1, L2, w1 and w2), makes this method efficient, and has the potential to be implemented into large-scale sediment transport models.

(3) The common standard deviation σ is modeled empirically as a function of the mean size of the entire FSD, the elementary particle size and a constant. In our applications, better agreements of

the modeled and measured FSDs are achieved by using an empirical σ rather than extracting σ from the (2N)th moment of FSD.

(4) High accuracy and robustness is not necessarily guaranteed if representing a simple FSD with excessive subordinate FSDs. It depends

on whether the shape of FSD is truly suitable to decompose into sub-components with the same σ.

(5) Future studies are needed to investigate the subordinate FSDs in stratified estuaries. Microbial processes or a second internal property (such as the floc density) in the PBE might be helpful to better address the properties of biomineral suspended particulate matters. Besides, numerical schemes of both explicit and implicit treatment of the flocculation kinetic terms are expected to coincide with the transport terms of the fluid and carrying particles.

Acknowledgement

We would like to thank three anonymous reviewers for their constructive comments. This research was funded by the BelSPO (Belgian Science Policy Office) within the framework of the BRAIN-BE (Belgian Research Action through Interdisciplinary Networks) INDI67 project (Developments of tools and methods to support the monitoring of EU Marine Strategy Framework Directive indicators 6 'Sea-floor integrity' and 7 'Hydrographical conditions' - Grant no. BR/143/A2/INDI67) and the JPI-OCEANS (The Joint Programming Initiative Healthy and Productive Seas and Oceans) WEATHER-MIC (How microplastic weathering changes its transport, fate and toxicity in the marine environment – Grant no. BR/154/A1/WEATHER-MIC).) project. The first author was also supported by the Open Research Fund of State Key Laboratory of Estuarine and Coastal Research of China (Grant No. SKLEC-KF201811).

References

Agrawal, Y.C., Pottsmith, H.C., 2000. Instruments for particle size and settling velocity observations in sediment transport. *Marine Geology* 168, 89−114.

Benson, T., French, J.R., 2007. InSiPID: A new low-cost instrument for in situ particle size measurements in estuarine and coastal waters. *Journal of Sea Research* 58, 167−188.

Cartwright, G.M., Friedrichs, C.T., Dickhudt, P.J., Gass, T., Farmer, F.H., 2009. Using the acoustic Doppler velocimeter (ADV) in the MUDBED real-time observing system. Proceedings, OCEANS 2009, Institute of Electrical and Electronics Engineers, ISBN 978-1-4244-4960-6, pp. 1428−1436.

Cartwright, G.M., 2013. Application of acoustics and optics for the characterization of suspended particulate matter within an estuarine observing system. (Ph.D. Dissertation) The College of William and Mary, Gloucester Point, Virginia.

Cuthbertson, A., Dong, P., King, S., Davies, P., 2008. Hindered settling velocity of cohesive/non-cohesive sediment mixtures. *Coastal Engineering* 55, 1197−1208.

Cuthbertson, A.J.S., Dong, P., Davies, P.A., 2010. Non-equilibrium flocculation characteristics of fine-grained sediments in grid-generated turbulent flow. *Coastal Engineering* 57, 447−460.

Cuthbertson, A.J.S., Samsami, F., Dong, P., 2018. Model studies for flocculation of sand-clay mixtures. *Coastal Engineering* 132, 13−32.

Ducoste, J.J., Clark, M.M., 1998.The influence of tank size and impeller geometry on turbulentflocculation: I. Experimental. *Environmental Engineering Science* 15, 215–224.

Eisma, D., Schuhmacher, T., Boekel, H., Van Heerwaarden, J., Franken, H., Laan, M., Vaars, A., Eijgenraam, F., Kalf, J., 1990. A camera and image-analysis system for in situ observations of flocs in natural waters. *Netherlands Journal of Sea Research* 27, 43−56.

Fettweis, M., Baeye, M., Cardoso, C., Dujardin, A., Lauwaerts, B., Van den Eynde, D., Van Hoestenberghe, T., Vanlede, J., Van Poucke, L., Velez, C., Martens, C., 2016. The impact of disposal of fine grained sediments from maintenance dredging works on SPM concentration and fluid mud in and outside the harbor of Zeebrugge. *Ocean Dynamics* 66, 1497−1516.

Fettweis, M., Lee, B.J., 2017. Spatial and seasonal variation of biomineral suspended particulate matter properties in high-turbid nearshore and low-turbid offshore zones. *Water* 9, 694.

Furukawa, Y., Watkins, J.L., 2012. Effect of Organic Matter on the Flocculation of Colloidal Montmorillonite: A Modeling Approach. *Journal of Coastal Research* 28, 726−737.

Graham, G.W., Nimmo Smith, W.A.M., 2010. The application of holography to the analysis of size and settling velocity of suspended cohesive sediments. *Limnology and Oceanography: Methods* 8, 1−15.

Guo, L., He, Q., 2011. Freshwater flocculation of suspended sediments in the Yangtze River, China. *Ocean Dynamics* 61, 371−386.

Guo, C., He, Q., Guo, L., Winterwerp, J.C., 2017. A study of in-situ sediment flocculation in the turbidity maxima of the Yangtze Estuary. *Estuarine, Coastal and Shelf Science* 191, 1−9.

Guo, C., He, Q., van Prooijen, B.C., Guo, L., Manning, A.J., Bass, S., 2018. Investigation of flocculation dynamics under changing hydrodynamic forcing on an intertidal mudflat. *Marine Geology* 395, 120−132.

He, Q., Guo, L., Liu, H., Wang, Y., 2015. Changjiang Estuary sediment transport dynamics. *In*: Ecological continuum from the Changjiang (Yangtze River) watersheds to the East China Sea continental margin. Springer International Publishing, pp. 47–69.

Keyvani, A., Strom, K., 2014. Influence of cycles of high and low turbulent shear on the growth rate and equilibrium size of mud flocs. *Marine Geology* 354, 1–14.

Laurent, L., Nguyen, T.T., 2017. Realizable second-order finite-volume schemes for the advection of moment sets of the particle size distribution. *Journal of Computational Physics* 337, 309−338.

Lee, B.J., Toorman, E., Molz, F.J., Wang, J., 2011. A two-class population balance equation yielding bimodal flocculation of marine or estuarine sediments. *Water Research* 45, 2131−2145.

Lee, B.J., Fettweis, M., Toorman, E., Molz, J., 2012. Multimodality of a particle size distribution of cohesive suspended particulate matters in a coastal zone. *Journal of Geophysical Research* 117, C03014.

Lee, B.J., Toorman, E., Fettweis, M., 2014. Multimodal particle size distributions of fine-grained sediments: mathematical modelling and field investigation. *Ocean Dynamics* 64, 429−441.

Lee, D.G., Bonner, J.S., Garton, L.S., Ernest, A.N.S., Autenrieth, B.L., 2000. Modeling coagulation kinetics incorporating fractal theories: a fractal rectilinear approach. *Water Research* 34, 1987–2000.

Letter, J.V., Mehta, A.J., 2011. A heuristic examination of cohesive sediment bed exchange in turbulent flows. *Coastal Engineering* 58, 779−789.

Madadi-Kandjani, E., Passalacqua, A., 2015. An extended quadrature-based moment method with log-normal kernel density functions. *Chemical Engineering Science* 131, 323−339.

Maggi, F., 2005. Flocculation dynamics of cohesive sediment. (Ph.D. Dissertation) Delft University of Technology, Netherlands.

Maggi, F., 2007.Variable fractal dimension: a major control for floc structure and flocculation kinematics of suspended cohesive sediment. *Journal of Geophysical Research* 112, C07012.

Magnus, W., Oberhettinger, F., Soni, R.P., 1966. Formulas and theorems for the special functions of mathematical physics. Springer-Verlag.

Manning, A.J., Dyer, K.R., 2002. A comparison of floc properties observed during neap and spring tidal conditions. *In*: J.C. Winterwerp and C. Kranenburg, (eds.), Fine Sediment Dynamics in the Marine Environment - Proceedings in Marine Science 5, Amsterdam: Elsevier, pp. 233-250.

Manning, A.J., 2004. Observations of the properties of flocculated cohesive sediment in three western European estuaries. *Journal of Coastal Research* SI 41, 70−81.

Marchisio, D.L., Barrsei, A.A., Baldi, G., Fox, R.O., 2002. Comparison between the classes method and the quadrature method of moments for multiphase systems. *In*: 8th Conference "Multiphase Flow in Industrial Plants", Alba, Italy, 2002.

Marchisio, D.L., Vigil, R.D., Fox, R.O., 2003a. Implementation of the quadrature method of moments in CFD codes for aggregation–breakage problems. *Chemical Engineering Science* 58, 3337−3351.

Marchisio, D.L., Vigil, R.D., Fox, R.O., 2003b. Quadrature method of moments for aggregation-breakage processes. *Journal of Colloid and Interface Science* 258, 322−334.

McGraw, R., 1997. Description of aerosol dynamics by the quadrature method of moments. *Aerosol Science and Technology* 27, 255–265.

Mehta, A.J., 2013. An Introduction to Hydraulics of Fine Sediment Transport. World Scientific Publishing Company.

Mhashhash, A., Bockelmann-Evans, B., Pan, S.Q., 2018. Effect of hydrodynamics factors on sediment flocculation processes in estuaries. *Journal of soils and sediments* 18, 3094−3103.

Mietta, F., Maggi, F., Winterwerp, J.C., 2008. Chapter 19: Sensitivity to breakup functions of a population balance equation for cohesive sediments. Proceedings in Marine Science 9, 275–286 (Sediment and Ecohydraulics - INTERCOH 2005).

Mietta, F., Chassagne, C., Verney, R., Winterwerp, J.C., 2011. On the behavior of mud floc size distribution: model calibration and model behavior. *Ocean Dynamics* 61, 257−271.

Mikkelsen,O.A., Hill, P.S., Milligan, T.G., Chant, R.J., 2005. In situ particle size distributions and volume concentrations from a LISST-100 laser particle sizer and a digital floc camera. *Continental Shelf Research* 25, 1959−1978.

Milliman, J.D., Shen, H., Yang, Z., Mead, R.H., 1985. Transport and deposition of river sediment in the Changjiang estuary and adjacent continental shelf. *Continental Shelf Research* 4, 37−45.

Mugele, R.A., Evans, H.D., 1951. Droplet size distribution in sprays. *Industrial and Engineering Chemistry* 43, 1317–1324.

Nguyen, T.T., Laurent, F., Fox, R.O., Massot, M., 2016. Solution of population balance equations in applications with fine particles: Mathematical modelling and numerical schemes. *Journal of Computational Physics* 325, 129−156.

Passalacqua, A., Laurent, F., Madadi-Kandjani, E., Heylmun, J.C., Fox, R.O., 2018. An open-source quadrature-based population balance solver for OpenFOAM. *Chemical Engineering Science* 176, 306−318.

Prat, O.P., Ducoste, J.J., 2006. Modeling spatial distribution of floc size in turbulent processes using the quadrature method of moment and computational fluid dynamics. *Chemical Engineering Science* 61, 75−86.

Press, W.H., Teukolsky, S.A., Vetterling, W.T., Flannery, B.P., 1992.Numerical Recipes in Fortran: The Art of Scientific Computing. Second ed. Cambridge University Press, Cambridge, United Kingdom.

Ramalingam, R., Chandra, V., 2017. Determination of suspended sediments particle size distribution using image capturing method. *Marine Georesources & Geotechnology*. DOI: 10.1080/1064119X.2017.1392660

Reochert, P., Omlon, M. (1996). On the usefulness of overparameterized ecological models. Ecological Modelling, 95:289-299.

Richardson, J.F., Zaki, W.N., 1954. Sedimentation and fluidisation: Part I. *Transactions of the Institution of Chemical Engineers and the Chemical Engineer* 32, 35−53.

Schaffner, L.C., Hinchey, E.K., Dellapenna, T.M., Friedrichs, C.T., Thompson Neubauer, M., Smith, M.E., Kuehl, S.A., 2001. Physical energy regimes, sea-bed dynamics and organism-sediment interactions along an estuarine gradient, *In*: Aller, J.Y., Woodin, S.A., Aller, R.C. (Eds.), Organism-Sediment Interactions, University of South Carolina Press, Columbia, SC, pp. 161−182.

Schoups, G., Van De Giesen, N. C., & Savenije, H. H. G. (2008). Model complexity control for hydrologic prediction. Water Resources Research,44, W00B03.

Shen, X., Maa, J.P.Y., 2015. Modeling floc size distribution of suspended cohesive sediments using quadrature method of moments. *Marine Geology* 359, 106−119.

Shen, X., Maa, J.P.Y., 2016a. A camera and image processing system for floc size distributions of suspended particles. *Marine Geology* 376, 132−146.

Shen, X., Maa, J.P.Y., 2016b. Numerical simulations of particle size distributions: Comparison with analytical solutions and kaolinite flocculation experiments. *Marine Geology* 379, 84−99.

Shen, X., Maa, J.P.Y., 2017. Floc size distributions of suspended kaolinite in an advection transport dominated tank: Measurements and modeling. *Ocean Dynamics* 67, 1495−1510.

Shen, X., Lee, B.J., Fettweis, M., Toorman, E.A., 2018a. A tri-modal flocculation model coupled with TELEMAC for estuarine muds both in the laboratory and in the field. *Water Research* 145, 473−486.

Shen, X., Toorman, E.A., Lee, B.J., Fettweis, M., 2018b. Biophysical flocculation of suspended particulate matters in Belgian coastal zones. *Journal of Hydrology* 567, 238−252.

Smoluchowski, M., 1917. Versuch einer Mathematischen Theorie der Koagulationskinetik Kolloider Lösungen. *Zeitschrift für Physikalische Chemie* 92, 129–168.

Song, D., Wang, X.H., Cao, Z., Guan, W., 2013. Suspended sediment transport in the Deepwater Navigation Channel, Yangtze River Estuary, China, in the dry season 2009: 1. Observations over spring and neap tidal cycles. *Journal of Geophysical Research: Oceans* 118, 5555−5567.

Sowa, W.A., 1992. Interpreting mean drop diameters using distribution moments. *Atomization and Sprays* 2, 1–15.

Su, J., Gu, Z., Li, Y., Feng, S., Xu, X.Y., 2007. Solution of population balance equation using quadrature method of moments with an adjustable factor. *Chemical Engineering Science* 62, 5897−5911.

Tang, F.H.M., Maggi, F., 2015. A laboratory facility for flocculation-related experiments. The University of Sydney. Report No. R952.

Toorman, E.A., 2012. Large-scale modelling of fine-grained sediment transport: Can we do any betters? 12th Journées Nationales Génie Côtier - Génie Civil, Cherbourg, France. DOI: 10.5150/jngcgc.2012.053-T.

Tran, D., Kuprenas, R., Strom, K., 2018. How do changes in suspended sediment concentration alone influence the size of mud flocs under steady turbulent shearing? *Continental Shelf Research* 158, 1−14.

Vale, H.M., McKenna T.F., 2005. Solution of the Population Balance Equation for Two-Component Aggregation by an Extended Fixed Pivot Technique. *Industrial & Engineering Chemistry Research* 44, 7885–7891.

Van Leussen, W., 1994. Estuarine macroflocs: Their role in fine-grained sediment transport. University of Utrecht, The Netherlands.

Vanni, M., 2000.Approximate population balance equations for aggregation-breakage processes. *Journal of Colloid and Interface Science* 221, 143–160

Verney, R., Lafite, R., Brun-Cottan, J.C., Le Hir, P., 2011. Behaviour of a floc population during a tidal cycle: laboratory experiments and numerical modelling. *Continental Shelf Research* 31, S64-S83.

Wheeler, J.C., 1974.Modified moments and Gaussian quadratures. *Journal of Mathematics* 4, 287–296.

Winterwerp, J.C., 1998. A simple model for turbulence induced flocculation of cohesive sediment. *Journal of Hydraulic Research* 36, 309–326.

Winterwerp, J.C., 2002. On the flocculation and settling velocity of estuarine mud. *Continental Shelf Research* 22, 1339−1360.

Wolanski, E., Elliott, M., 2016. Estuarine sediment dynamics. *In*: Estuarine Ecohydrology - An Introduction (2nd Eds.), Amsterdam: Elsevier, pp. 77–125.

Wright, D.L., 2007. Numerical advection of moments of the particle size distribution in Eulerian models. *Journal of Aerosol Science* 2007, 352−369.

Yuan, C., Fox, R.O., 2011.Conditional quadrature method of moments for kinetic equations. *Journal of Computational Physics* 230, 8216–8246.

Yuan, C., Laurent, F., Fox, R.O., 2012. An extended quadrature method of moments for population balance equations. *Journal of Aerosol Science* 51, 1−23.

Zhang, J.F., Maa, J.P.Y., Zhang, Q.H., Shen, X.T., 2016. Direct numerical simulations of collision efficiency of cohesive sediments. *Estuarine, Coastal and Shelf Science* 178, 92−100.

Zhang, J.F., Zhang, Q.H., Maa, J.P.Y., Qiao, G.Q., 2017. Lattice Boltzmann simulations of oscillating-grid turbulence. *Journal of Hydrodynamics* 29, 68−74.

Zhang, J.-F., Zhang, Q.-H., Maa, J.P.-Y., 2018. Coagulation processes of kaolinite and montmorillonite in calm, saline water. *Estuarine Coastal and Shelf Science* 202, 18−29.

Zhu, Z., Xiong, X., Liang, C., Zhao, M., 2018. On the flocculation and settling characteristics of low- and high-concentration sediment suspensions: effects of particle concentration and salinity conditions. *Environmental Science and Pollution Research* 25, 14226–14243.

Table 1 Summary of model parameters and results for different guar gum dosages in the mixing jar tests, with initial suspended sediment concentration c = 0.52 g/L and tank averaged shear rate G = 55 s^{-1}.

Case	C_{guar} (mg/L)	α	E_b	α_0	n_f	L_1 (μm)	L_2 (μm)	w_1	w_2	σ	D_{50} (μm)	FSD Error
1	0	0.8	4.8E−6	0.162	2.8	32.9	110.0	0.73	0.27	0.5874	21.6	0.0714
2	5	0.8	3.5E−6	0.162	2.7	34.2	104.3	0.65	0.35	0.5794	23.7	0.0552
3	10	0.8	2.4E−6	0.166	2.65	31.9	100.5	0.45	0.55	0.6168	24.4	0.0490
4	15	0.8	1.0E−6	0.150	2.6	37.1	151.2	0.31	0.69	0.6297	32.6	0.0587
5	20	0.8	2.0E−6	0.165	2.7	29.8	113.3	0.34	0.66	0.6605	24.4	0.0367
6	30	0.8	3.9E−6	0.181	2.8	25.1	85.8	0.43	0.57	0.6872	18.3	0.0285

Table 2 Parameters used in the best-quality simulation for the settling column experiment.

Symbol	Value	Description
c	0.5	Initial suspended sediment concentration (g/L)
G	5, 10, 20, 40	Shear rate generated by the oscillating grids in the settling section (s^{-1})
N_d	2	Number of lognormal distributions
N_{di}	3	Number of pivots for each subordinate lognormal distribution
α	0.95†	Collision efficiency
E_b	1.05E−5	Breakage fitting parameter
α_0	0.195†	Coefficient for computing the shared standard deviation for all subordinate lognormal distributions
n_f	2.3	Fractal dimension
K	5	Coefficient in the fragmentation distribution function
l_p	8	Size of primary particles (μm)
c_{gel}	40	Gelling concentration (g/L)
F_y	1.0E−10	Floc strength (Pa)
Δt	0.1	Time step (s)
Δz	0.1	Vertical resolution (m)
n_z	50	Number of cells in the vertical direction.

† For shear rate $G = 5\ s^{-1}$, model results are recalibrated by setting $\alpha = 1.1$ and $\alpha_0 = 0.175$.

Figures

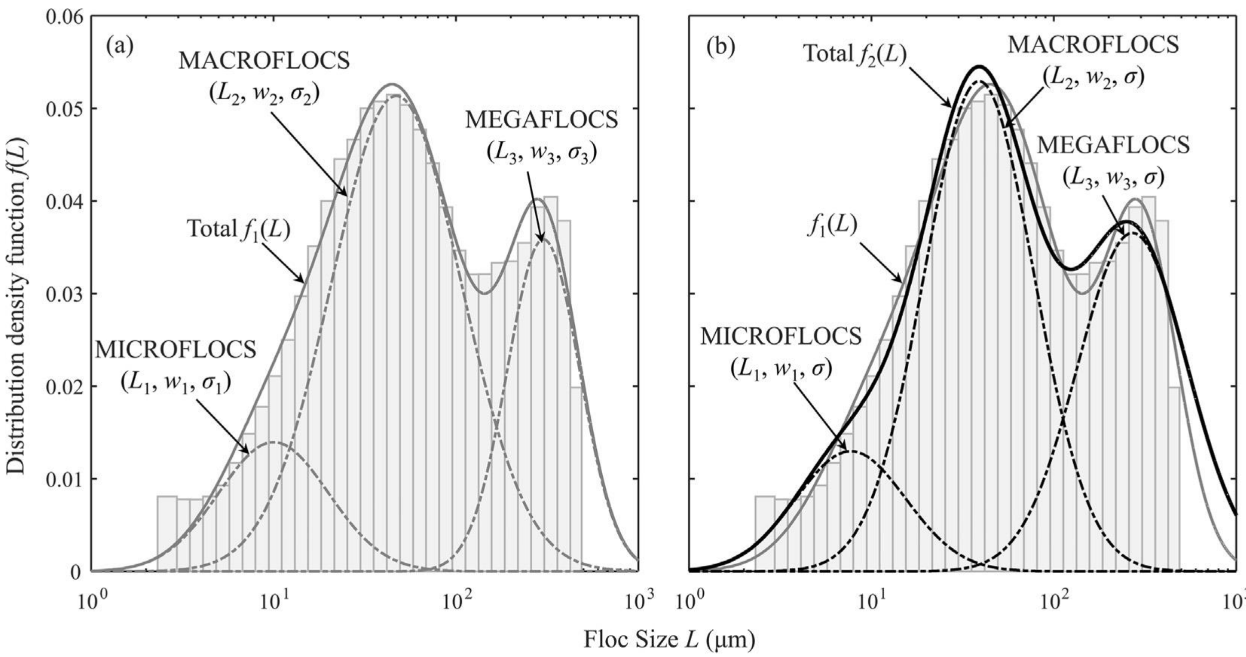

Fig. 1 An example of decomposing a measured FSD into three lognormal distributions for microflocs L_1, macroflocs L_2 and megaflocs L_3. Subordinate FSDs (a) with varying standard deviations (σ_1, σ_2, σ_3) and (b) with a common standard deviation σ are compared. The bars represent a typical FSD collected by LISST at site MOW1 at Belgian coast. Dashdotted lines are subordinate FSDs and the solid line is the superposed FSD. The entire FSD $f_1(L)$ in subfigure (a) is also plotted in subfigure (b) for comparsion.

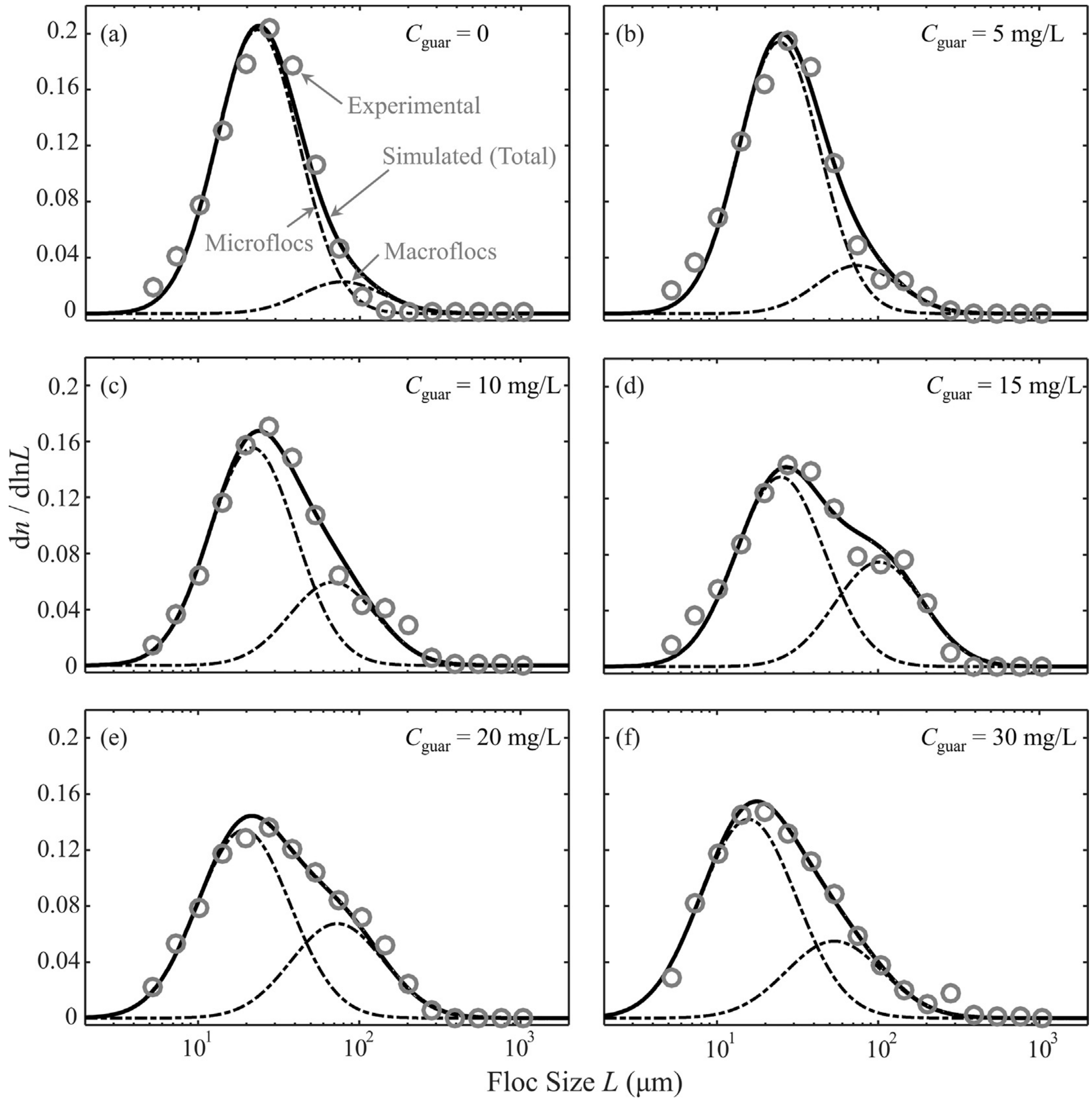

Fig. 2 Comparison of simulated and observed FSDs for guar gum concentration c_{guar} = {0, 5, 10, 15, 20, 30} mg/L in the mixing jar experiments. Symbols are measurements and dark solid lines are the modeled FSDs, with two subordinate lognormal distributions marked with dashdotted lines.

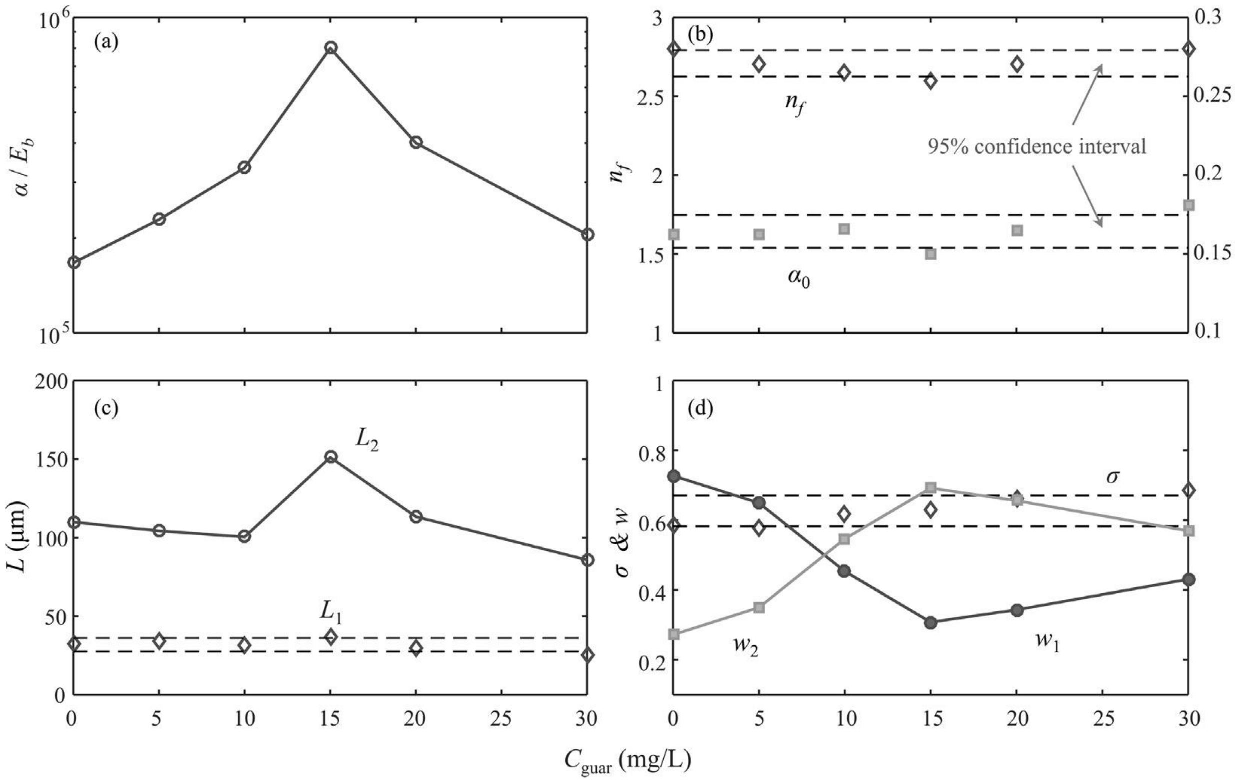

Fig. 3 Model parameters of (a) the ratio α/E_b, (b) the fractal dimension n_f and the standard deviation computing coefficient α_0, (c) the predicted representative sizes L_i, and (d) the corresponding weights w_i and the common standard deviation σ, for c_{guar} = {0, 5, 10, 15, 20, 30} mg/L in the mixing jar experiments.

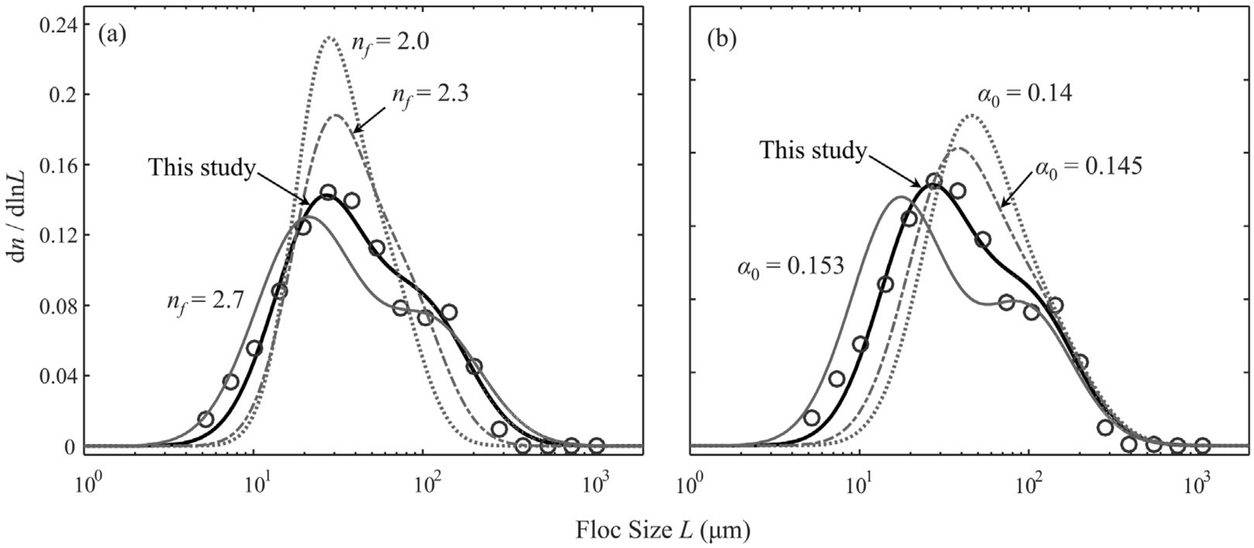

Fig. 4 Sensitivity tests of (a) fractal dimension n_f and (b) standard deviation computing coefficient α_0, for c_{guar} = 15 mg/L in the mixing jar experiment.

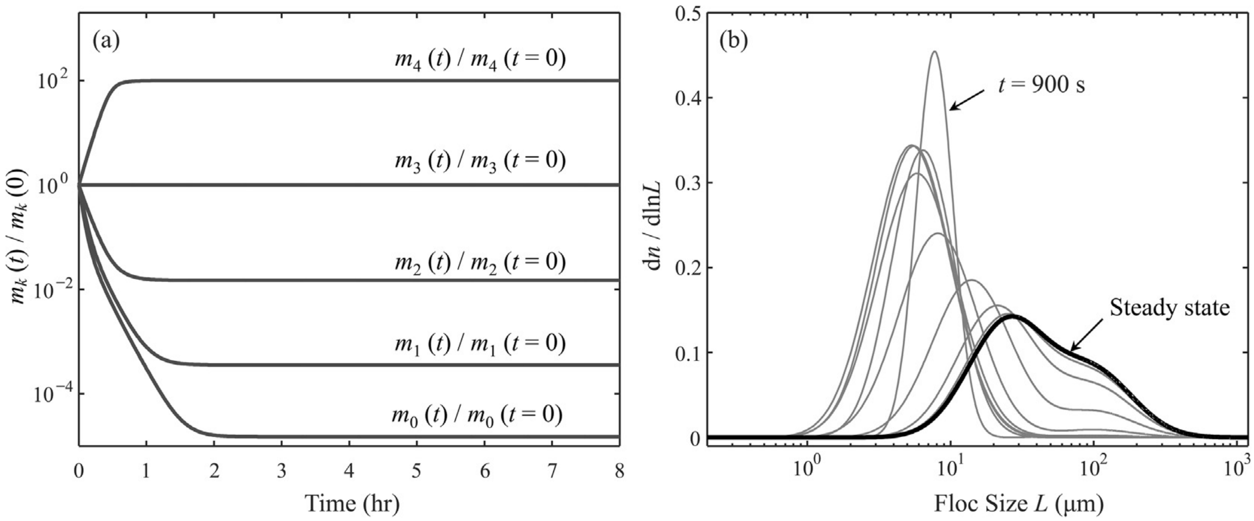

Fig. 5 (a) Time evolutions of the predicted moments m_k (k = 0, 1, 2, 3, 4) and (b) the predicted FSDs shown every 15 mins, for c_{guar} = 15 mg/L in the mixing jar experiment.

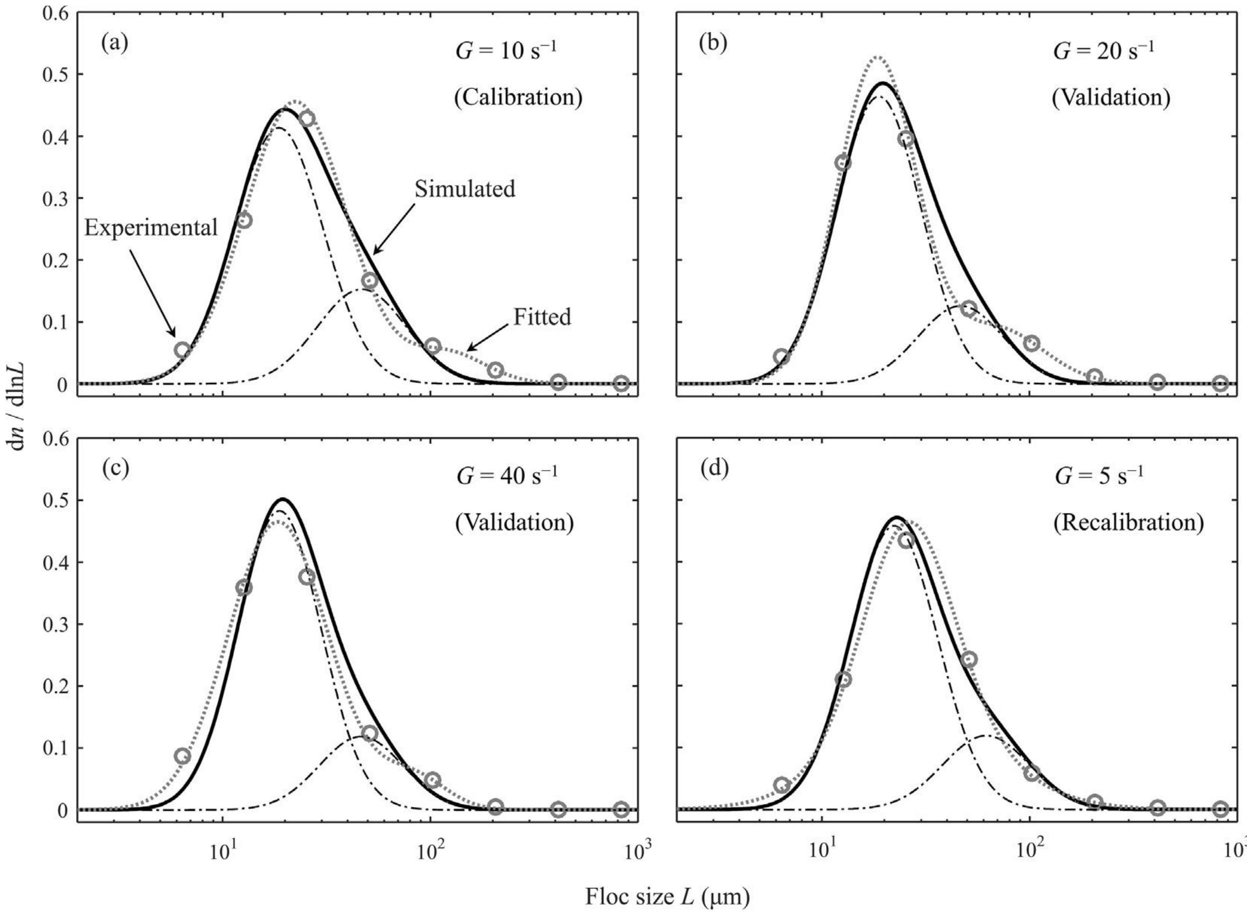

Fig. 6 Comparison of simulated and measured FSDs in the settling column tests for initial sediment concentration c = 0.5 g/L and shear rate G = {5, 10, 20, 40} s^{-1}. Symbols are measurements, dotted lines are fitted FSDs by software DistFit (treated as reference FSDs), dash-dotted lines are two modeled subordinate FSDs and the dark solid lines are the superposed predictions.

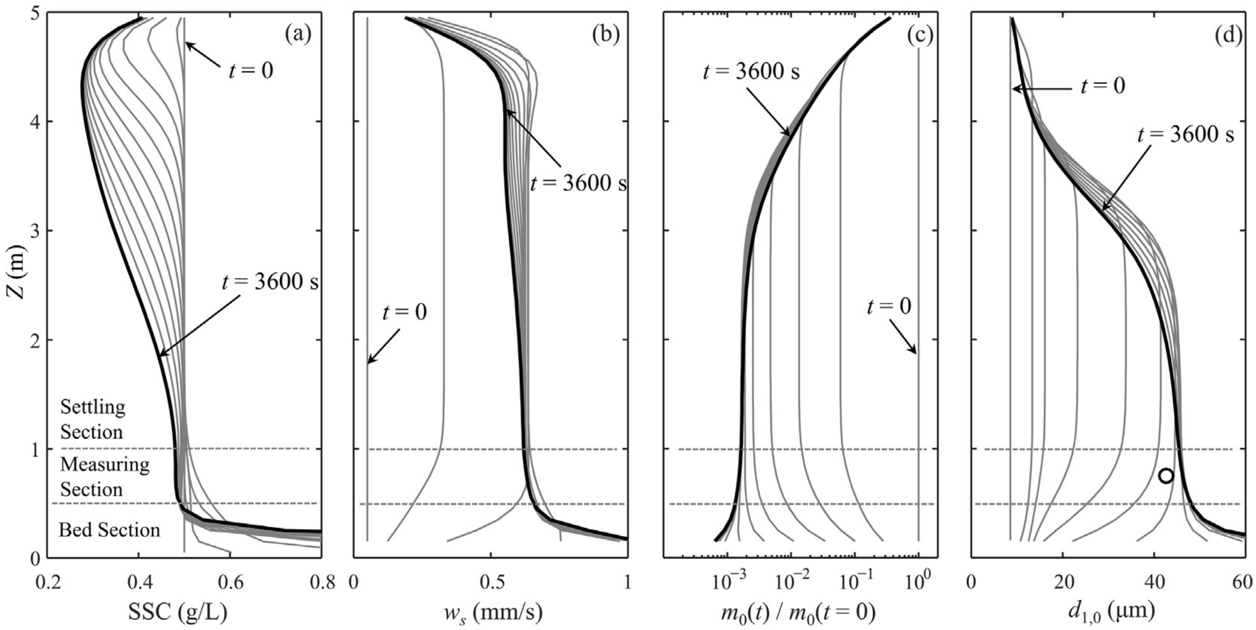

Fig. 7 Vertical profiles of (a) SSC, (b) settling velocity (w_s), (c) total particle number (m_0) and (d) mean size ($d_{1,0}$), for shear rate G = 10 s^{-1} in the settling column experiment.

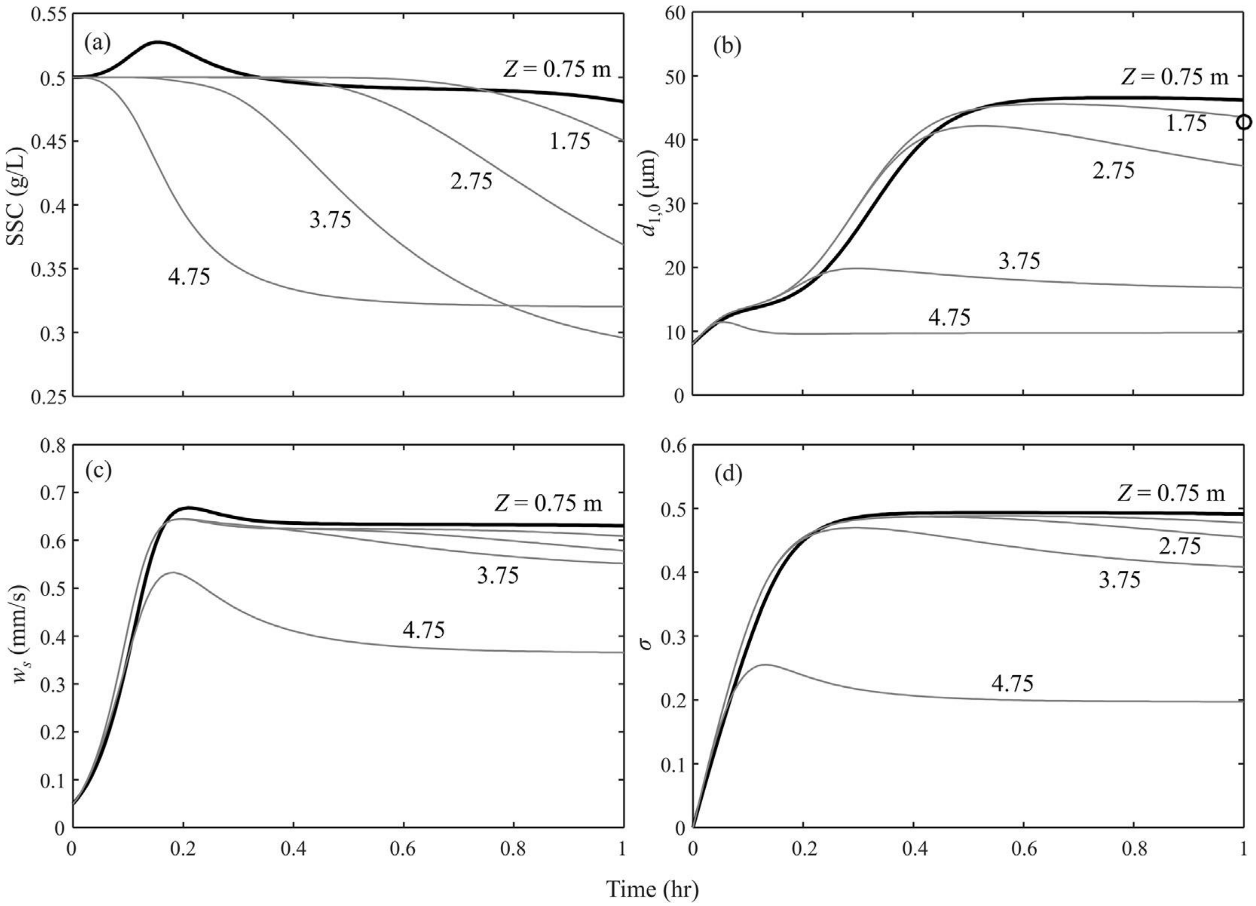

Fig. 8 Time evolutions of (a) SSC, (b) means size ($d_{1,0}$), (c) settling velocity (w_s) and (d) standard deviation (σ) at column height $Z = \{0.75, 1.75, 2.75, 3.75, 4.75\}$ m, for shear rate $G = 10$ s^{-1} in the settling column experiment. The symbol in subfigure (b) is the observed $d_{1,0}$ at the measuring section.

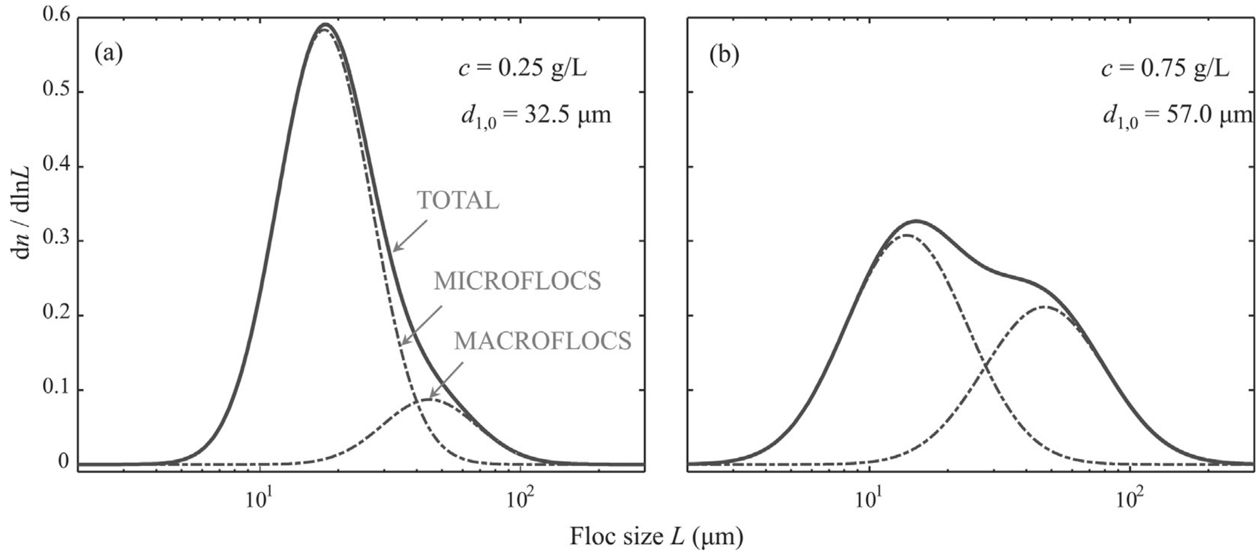

Fig. 9 Predicted FSDs for initial sediment concentrations (a) c = 0.25 g/L and (b) c = 0.75 g/L. The dark solid line is the modeled FSDs, with two subordinate FSDs marked with dash-dotted lines.